Convectons and secondary snaking in three-dimensional natural doubly diffusive convection

Cédric Beaume,[1,a)] Alain Bergeon,[1,b)] and Edgar Knobloch[2,c)]
[1]*Université de Toulouse, INPT, UPS, IMFT (Institut de Mécanique des Fluides de Toulouse), Allée Camille Soula, F-31400 Toulouse, France and CNRS, IMFT, F-31400 Toulouse, France*
[2]*Department of Physics, University of California, Berkeley, California 94720, USA*

Natural doubly diffusive convection in a three-dimensional vertical enclosure with square cross-section in the horizontal is studied. Convection is driven by imposed temperature and concentration differences between two opposite vertical walls. These are chosen such that a pure conduction state exists. No-flux boundary conditions are imposed on the remaining four walls, with no-slip boundary conditions on all six walls. Numerical continuation is used to compute branches of spatially localized convection. Such states are referred to as convectons. Two branches of three-dimensional convectons with full symmetry bifurcate simultaneously from the conduction state and undergo homoclinic snaking. Secondary bifurcations on the primary snaking branches generate secondary snaking branches of convectons with reduced symmetry. The results are complemented with direct numerical simulations of the three-dimensional equations.

I. INTRODUCTION

Doubly diffusive convection arises when two different fields diffuse at different rates. In the classic configuration, a horizontal layer containing a two-component fluid is heated from below and cooled from above. Different concentrations of the heavier component may be imposed at the boundaries or maintained by the Soret effect in response to the imposed temperature difference. Since heat diffuses more rapidly than concentration, diffusion-driven instabilities may occur in configurations which would otherwise be stable. Systems of this type are known to exhibit a wealth of behavior ranging from stationary and time-periodic patterns to chaotic solutions.[1–5] The case in which the concentration is destabilizing while the temperature field is stabilizing gives rise to the salt finger instability that is of considerable interest in oceanography,[6–9] geophysics,[10] and in the form of the Goldreich-Schubert-Fricke instability in astrophysics as well.[11] The opposite case, with destabilizing temperature and stabilizing concentration, also arises in oceanography and typically generates oscillations.[1,3]

In the above configurations, the driving gradients are parallel to the buoyancy force. In many situations of geophysical and astrophysical interest, these gradients are not aligned, however, and the case in which the gradients are orthogonal is often considered as representative.[12–14] The resulting configuration arises not only in oceanography,[9] but also in a variety of solidification processes[15] and is referred to as natural doubly diffusive convection.

In doubly diffusive convection, the relative influence of the imposed temperature and concentration gradients is quantified via the buoyancy ratio $N = \rho_C \Delta C / \rho_T \Delta T$, where ρ is the fluid density, $\rho_T \equiv \partial\rho/\partial T < 0$, $\rho_C \equiv \partial\rho/\partial C > 0$, and $\Delta T > 0$, $\Delta C > 0$ are, respectively, the differences in

[a)]Electronic mail: ced.beaume@gmail.com.
[b)]Electronic mail: alain.bergeon@imft.fr.
[c)]Electronic mail: knobloch@berkeley.edu.

the temperature and the concentration between a pair of opposite walls, both maintained at fixed temperature and concentration. Thus, $N > 0$ implies that both contributions to the buoyancy force cooperate, while $N < 0$ indicates competing contributions. The latter case generally produces richer dynamics and is the case of interest here.

The present study is motivated by the recent discovery of convectons, i.e., spatially isolated convection rolls, in two-dimensional (2D) spatially extended natural doubly diffusive convection.[16,17] We extend here this work to three-dimensional (3D) enclosures in order to study the effect of the third dimension on the form and stability of the existing solutions, and to identify new types of localized fully three-dimensional patterns. Our work builds on earlier work on 3D states in small enclosures[18] as explained further below. Throughout the paper, we find it useful to compare our results with those obtained for the much simpler Swift-Hohenberg equation. This nonlinear equation is of fourth-order in one spatial variable, and exhibits in appropriate situations bistability between a spatially periodic state and the trivial state. This bistability region in turn contains a "pinning" region with coexisting spatially localized states of different spatial extent, as well as bound states of such localized states. The term "localized" is used here to describe solutions consisting in a few oscillations, typically located in the center of the domain, that are embedded in a spatially uniform background, much as convectons consist of localized convection rolls embedded in a background conduction state. The localized states in the pinning region are organized in a snakes-and-ladders structure comprising a pair of intertwined branches of symmetric states connected by "rungs" consisting of asymmetric states, as described by Burke and Knobloch[19–21] and Beck *et al.*[22] Localized solutions have also been found in the buckling of slender structures where the preferred buckling mode may be localized in space,[23] in a variety of systems arising in nonlinear optics,[24] as well as in magnetoconvection[25,26] and shear flow.[27] Remarkably, many of these systems exhibit the same mathematical characteristics as the Swift-Hohenberg equation. This is so for doubly diffusive convection as well.[5,17,28,29]

Following the approach in Ref. 18, we study the case $N = -1$. In the presence of periodic boundary conditions, this case admits a trivial conduction state as well as the subcritical bifurcation to periodic states required for the presence of bistability. With the realistic closed container boundary conditions used here, this picture is necessarily modified[30] since periodic states are no longer present. To determine the resulting bifurcation diagram in three spatial dimensions, we compute stationary solutions of the equations via a continuation algorithm based on a Newton solver for the time-independent version of the equations of motion with the same boundary conditions, as first described by Tuckerman,[31] and Mamun and Tuckerman.[32] The equations are solved using the first-order scheme proposed by Karniadakis *et al.*[33] based on a spectral element spatial discretization. Further details of the numerical method can be found in Ref. 18.

In Sec. II, we formulate the problem and in Sec. III, we describe our continuation results. Section IV describes the results of direct numerical simulations of the governing equations and compares them with the continuation results. Brief conclusions follow in Sec. V.

II. MATHEMATICAL FORMULATION

We consider a two-component fluid in competing horizontal gradients of temperature and concentration. These gradients are imposed via Dirichlet-type boundary conditions applied on vertical walls at $z = 0, l$: the left wall ($z = 0$) is maintained at fixed temperature $T^* = T_r$ and concentration $C^* = C_r$ while the right wall ($z = l$) is maintained at temperature $T^* = T_r + \triangle T$ and concentration $C^* = C_r + \triangle C$, with $\triangle T > 0$, $\triangle C > 0$. We nondimensionalize the equations using l for lengths, $\triangle T$ for the temperature, $\triangle C$ for the concentration, and l^2/κ for time, where κ is the thermal diffusivity. We do not take into account cross-diffusion effects and use the Boussinesq approximation to expand the fluid density about the reference values T_r and C_r,

$$\rho(T^*, C^*) = \rho_0 + \rho_T(T^* - T_r) + \rho_C(C^* - C_r), \tag{1}$$

where T^* and C^* are, respectively, the dimensional temperature and concentration of the heavier fluid component, ρ_0 is the fluid density at the reference temperature T_r and concentration C_r, and $\rho_T < 0$ and $\rho_C > 0$ denote the thermal and solutal "expansion" coefficients, also at T_r and C_r. The mathematical model consists of the incompressible Navier-Stokes equation coupled to equations for

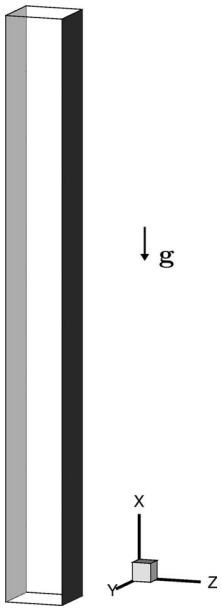

FIG. 1. Sketch of the vertically extended enclosure. The boundary conditions are no-slip for the velocity everywhere, no-flux for the temperature and concentration on all walls except for $T = C = 0$ at $z = 0$ (section represented in light gray) and $T = C = 1$ at $z = 1$ (section represented in dark gray).

the temperature and concentration. The nondimensionalized equations read

$$Pr^{-1}[\partial_t \mathbf{u} + (\mathbf{u} \cdot \nabla)\mathbf{u}] = -\nabla p + Ra(T - C)\hat{\mathbf{x}} + \nabla^2 \mathbf{u}, \tag{2}$$

$$\nabla \cdot \mathbf{u} = 0, \tag{3}$$

$$\partial_t T + (\mathbf{u} \cdot \nabla)T = \nabla^2 T, \tag{4}$$

$$\partial_t C + (\mathbf{u} \cdot \nabla)C = \tau \nabla^2 C, \tag{5}$$

where $\mathbf{u} \equiv (u, v, w)$ is the velocity field, p is the pressure and we have written $T = (T^* - T_r)/\triangle T$, $C = (C^* - C_r)/\triangle C$. The symbol $\hat{\mathbf{x}}$ denotes the unit vector in the vertical direction. Three parameters have been defined: the Rayleigh number $Ra = g|\rho_T|\triangle T l^3/\nu\kappa$, the Prandtl number $Pr = \nu/\kappa$, and the (inverse) Lewis number $\tau = D/\kappa$. Here, g is the gravitational acceleration while ν is the kinematic viscosity and D is the solutal diffusivity.

In this section, we consider the vertically extended enclosure sketched in Fig. 1. The enclosure is taken to be a closed container with square cross-section in the horizontal, and no-slip boundary conditions on the velocity are imposed on all six walls. The $z = 0$ wall is maintained at lower temperature and concentration $T = C = 0$ while the $z = 1$ wall is maintained at the higher values $T = C = 1$. These boundary conditions are responsible for setting up the gradients of temperature and concentration that drive the fluid motion. Boundary conditions on the temperature and concentration in the x and y directions are taken to be of no-flux type.

With these boundary conditions, the system (2)–(5) admits the trivial solution $\mathbf{u} = 0$, $T = C = z$, hereafter the conduction state. The equations for the perturbations $\mathbf{u}$, $\Theta \equiv T - z$ and $\Sigma \equiv C - z$ of this state are equivariant with respect to the following two symmetries:

$$S_y : (x, y, z) \to (x, 1 - y, z),\ (u, v, w, \Theta, \Sigma) \to (u, -v, w, \Theta, \Sigma), \tag{6}$$

$$S_\triangle : (x, y, z) \to (-x, y, 1 - z),\ (u, v, w, \Theta, \Sigma) \to -(u, -v, w, \Theta, \Sigma). \tag{7}$$

As a result, the equations for the perturbations $(\mathbf{u}, \Theta, \Sigma)$ possess D_2 symmetry, where $D_2 = \{1, S_y, S_\triangle, S_c\}$. Here, $S_c = S_y \circ S_\triangle = S_\triangle \circ S_y$ represents center symmetry, i.e., reflection with respect to the center of the enclosure. The conduction state has the full symmetry D_2. Instabilities of this state may either respect this symmetry or break it. One finds that there are two types of primary instabilities, those that respect D_2 and those that break the symmetry $S_\triangle$ of the conduction state. The former bifurcate from the conduction state in a transcritical bifurcation, while the latter bifurcate in a pitchfork bifurcation. The neutral curves corresponding to these instabilities are intertwined as a function of the aspect ratio L of the container. As a result for certain intervals of L, the transcritical bifurcation precedes the pitchfork while for others the pitchfork precedes the transcritical bifurcation.[18] Primary instabilities breaking the symmetry S_y occur at much larger Rayleigh numbers and are not of interest in the present work.

III. RESULTS

In the following, we present results obtained for the physical parameters used by Bergeon and Knobloch:[18] $Pr = 1$ and $\tau = 1/11$, but choose the aspect ratio L such that the enclosure contains 8 critical wavelengths of the 2D linear problem, $L = 19.8536$, see Xin *et al.*[14] We use the Rayleigh number Ra as a continuation parameter. All solutions have been computed with a spatial discretization that uses 16 spectral elements with $21 \times 19 \times 19$ points each.

A. Primary snaking

The conduction state remains stable until Ra reaches the value $Ra_p \approx 850.78$ at which a steady-state pitchfork bifurcation takes place. The marginal mode $\tilde{f}_p \equiv (\tilde{u}_p, \tilde{v}_p, \tilde{w}_p, \tilde{T}_p, \tilde{C}_p)$ related to this bifurcation is shown in Fig. 2(a). The eigenfunction satisfies $S_y \tilde{f}_p = \tilde{f}_p$, $S_\triangle \tilde{f}_p = -\tilde{f}_p$. Because of this symmetry, the two branches of the pitchfork are related by symmetry and hence appear as a single branch in the bifurcation diagram (not shown). As suggested by linear stability theory and confirmed by Bergeon and Knobloch,[18] the extent of this branch is very narrow and the branch terminates almost immediately on a subcritical branch of D_2 symmetric states emanating from the next primary bifurcation, a transcritical bifurcation, and labeled L^+ in Fig. 3. As the aspect ratio changes, the bifurcations remain close although their order may change.[34]

The transcritical bifurcation takes place at $Ra = Ra_t \approx 850.86$ and is shown in Fig. 3. The mode responsible for this instability, $\tilde{f}_t \equiv (\tilde{u}_t, \tilde{v}_t, \tilde{w}_t, \tilde{T}_t, \tilde{C}_t)$, is represented in Fig. 2(b) and satisfies $S_y \tilde{f}_t = \tilde{f}_t$, $S_\triangle \tilde{f}_t = \tilde{f}_t$, i.e., the instability at Ra_t does not break the symmetry of the conduction state. The resulting bifurcation must therefore be transcritical[18] although here it is only very weakly so because of the large aspect ratio of the domain. Consequently, the supercritical branch turns towards smaller values of Ra almost immediately and the bifurcation at Ra_t looks like a pitchfork bifurcation. However, at larger amplitude the two branches $L^\pm$ that result are manifestly unrelated by symmetry (Figs. 2 and 3).

As one follows the branches $L^\pm$ to larger amplitude, the solution changes rapidly from counter-rotating rolls[35,36] that vanish at the boundaries of the domain to one favoring rolls with upward flow near the hotter wall, i.e., a solution consisting of corotating rolls. This nonlinear effect, described by Thangam *et al.*,[37] is a consequence of the fact that heat diffuses faster than concentration. In addition, the presence of the lower and upper walls weakens the flow near these boundaries resulting finally in a modulated array of corotating rolls. The amplitude of this modulation increases rapidly with the roll strength resulting in strongly spatially localized structures. Of these, L^+ consists of a single roll at the center of the enclosure while L^- consists of a pair of corotating rolls, also at the center of the enclosure (Figs. 2(b1) and 2(b2)). Observe that in contrast to the situation with periodic boundary conditions in the vertical direction the branches of localized states are no longer secondary branches that bifurcate from a branch of periodic states[30,38] but are now *primary* branches that connect directly to the primary bifurcation. This is a consequence of the boundary layers at the top and bottom of the enclosure.

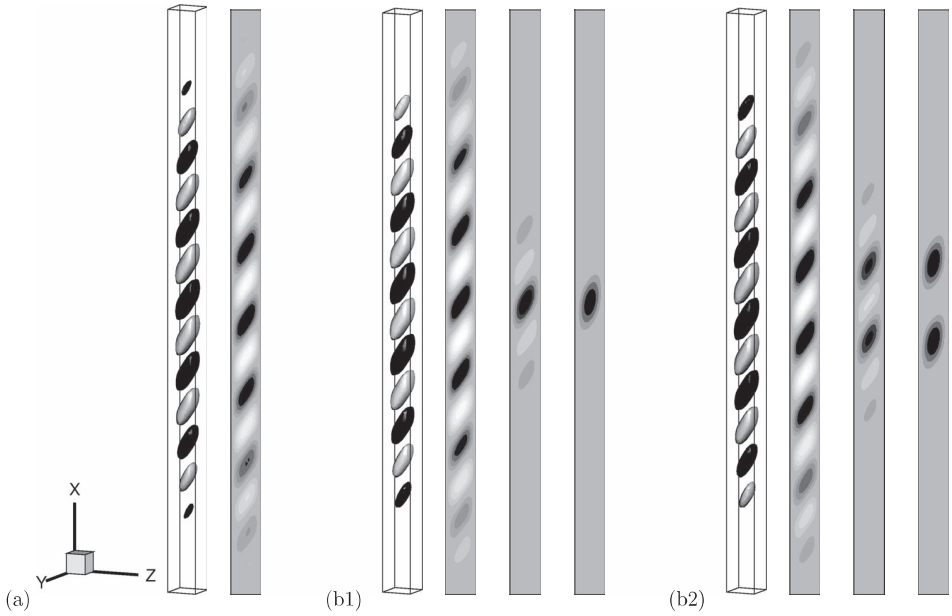

FIG. 2. Representation of the eigenmodes responsible for the first two instabilities. (a) Marginal eigenmode $\tilde{f}_p$ at the pitchfork bifurcation represented by isosurfaces $w = \pm W$ with W chosen appropriately (light indicates $w = W > 0$ while dark indicates $w = -W < 0$) and by the isovalues of the streamfunction in the plane $y = 1/2$ (light indicates clockwise motion while dark indicates counterclockwise motion). (b1) Similar representation of the marginal eigenmode $\tilde{f}_t$ at the transcritical bifurcation (Fig. 3). The last two panels show the evolution of the corresponding nonlinear solution along the branch L^+ using isovalues of the streamfunction in the plane $y = 1/2$ at $Ra \approx 810$ and $Ra \approx 740$. (b2) As in (b1) but showing the branch L^- corresponding to the eigenfunction $-\tilde{f}_t$.

Figure 4 shows the subsequent evolution of the $L^\pm$ branches projected onto the total kinetic energy

$$E = \frac{1}{2}\int_0^1 \int_0^1 \int_{-L/2}^{L/2} (u^2 + v^2 + w^2)\, dx\, dy\, dz. \tag{8}$$

The localized states shown in Figs. 2(b1) and 2(b2) correspond to solutions on the lowest part of each branch and reveal increasing localization with increasing amplitude (decreasing Rayleigh number); with further increase in amplitude as measured by the kinetic energy E both branches undergo snaking, but the details are quite different. Figure 4(a) shows that the L^+ branch executes three back and forth oscillations in a well-defined interval of Rayleigh numbers, $703 < Ra < 807$, before

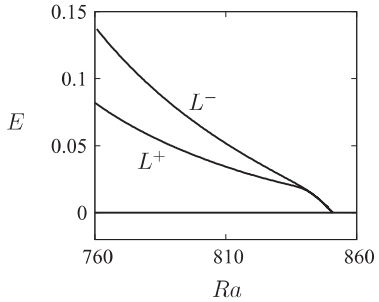

FIG. 3. Bifurcation diagram near the primary transcritical bifurcation showing the kinetic energy E as a function of the Rayleigh number Ra along the L^+ and L^- branches. The L^- branch bifurcates towards larger Ra but turns around almost immediately in a saddle-node bifurcation that occurs at a very low amplitude. As a result, the two branches appear indistinguishable on the scale of the figure.

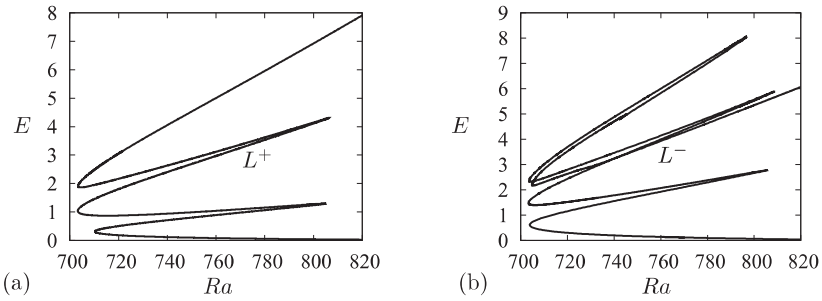

FIG. 4. Bifurcation diagrams representing the kinetic energy E as a function of the Rayleigh number Ra along the (a) L^+ branch and (b) L^- branch. The solutions at each saddle-node are represented in Figs. 5(a) and 5(b). The L^+ branch consists of solutions with an odd number of convection rolls. The oscillations in the branch are associated with the nucleation of new rolls at either side of the structure (left edge of the snaking region) and their growth towards full amplitude (right edge). The repeated nucleation of rolls ends when five rolls are present and the container is full after which the energy E increases monotonically with Ra. The L^- branch consists of solutions with an even number of rolls but instead of increasing monotonically after the container is full the L^- branch turns back towards smaller energies and the solution splits into a two-pulse state with a defect in the center of the domain before leaving the snaking region.

reaching larger Ra values. As shown in Fig. 5(a), the oscillations are a consequence of the growth of the localized structure: near each left saddle-node the structure nucleates a pair of corotating rolls, one roll on either side of the existing structure, and these rolls then strengthen as Ra increases. At the same time, their wavelength increases substantially. Once the structure fills the enclosure, the back and forth oscillations of the branch cease and the branch continues to larger values of Ra, instead of terminating in a secondary bifurcation on a branch of periodic states as in the case with periodic boundary conditions.[17,39] The localized states along the large Ra part of the branch resemble a periodic structure with defects due to the top and bottom boundaries, and play the role of the large amplitude periodic states present with periodic boundary conditions. Overall, the L^+ branch behaves much like the corresponding branch in binary fluid convection in a closed horizontal container.[30,40]

The behavior of the L^- branch initially follows that of the L^+ branch (Fig. 4(b)) but once the enclosure is filled with six large rolls (snapshot 6 in Fig. 5(b)), the branch instead turns back towards smaller Ra and the rolls begin to weaken again. Near $Ra \approx 745$, the branch passes through a pair of nearby folds (omitted from Fig. 5) near which the solution begins to split into a pair of three-roll states separated by a conduction region, i.e., into a two-pulse state.[5,26] Snapshot 7 in Fig. 5(b) shows

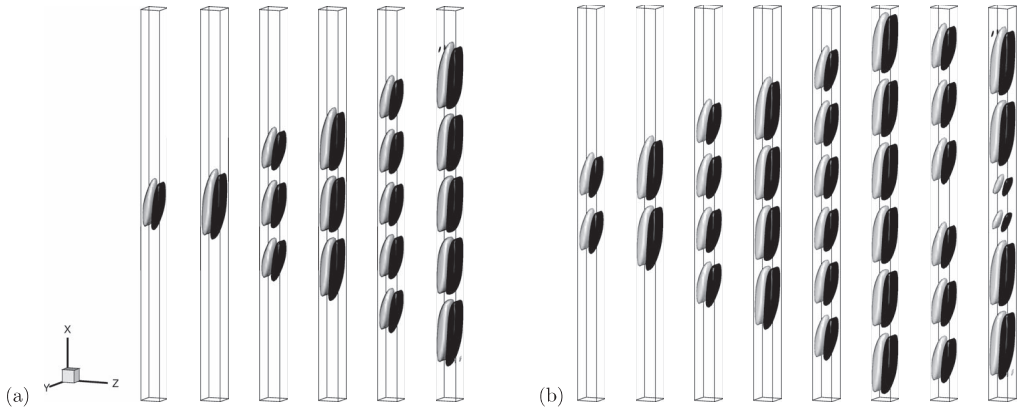

FIG. 5. Solutions at successive saddle-nodes in the bifurcation diagrams in Fig. 4. (a) L^+ branch, (b) L^- branch. The solutions are ordered from left to right in terms of increasing distance from the primary bifurcation at $Ra_t \approx 850.86$. The solutions are shown in terms of surfaces of constant vertical velocity, $u = \pm U$, with U chosen appropriately (light indicates $u = -U < 0$ while dark indicates $u = U > 0$). The last snapshot in (a) is taken at $Ra \approx 841$ and that in (b) at $Ra \approx 840$. In each roll, the flow is upwards near the $z = 1$ wall and downwards near $z = 0$.

the solution that results at the next left-most saddle-node. Beyond this fold, the solution strengthens monotonically with increasing Ra, with the outer pair of cells in each pulse growing at the expense of the cells nearest the center (snapshot 8 in Fig. 5(b), $Ra \approx 840$); with further increase in Ra these two inner cells vanish leaving a pair of two-cell states. This transition is not associated with additional folds and the two-pulse branch exits the snaking region in a monotonic fashion.

The behavior just described bears some similarity with that observed in the Swift-Hohenberg equation with a quadratic-cubic nonlinearity when this equation is posed on a finite interval with Robin boundary conditions at either end. When these boundary conditions are chosen to respect the reflection symmetry $x \to -x$ of the equation one finds that the standard snakes-and-ladders structure of the pinning region breaks up[38] in a way that is similar to that observed in the present 3D hydrodynamics problem. Specifically, Fig. 7 of Ref. 38 shows a weakly transcritical bifurcation that also looks like a pitchfork on a slightly larger scale just as in the present system. The bifurcation produces a branch labeled $S_{6,0}$ containing six basic wavelengths that bifurcates subcritically and plays the role of L^+. Indeed, Fig. 6 of Ref. 38 shows that this branch behaves at large amplitude in an identical manner to that shown in Fig. 4(a). In particular, the localized states bifurcate directly from the trivial state and transition smoothly and continuously into large amplitude defect states, exactly as here. In addition, Figs. 7 and 9 of Ref. 38 show that the supercritical branch labeled $S_{6,\pi}$ becomes subcritical almost immediately and thereafter behaves much like the L^- branch in the present work. In particular, the branch $S_{6,\pi}$ also starts to snake back towards small amplitude and exhibits a pair of nearby folds (Figs. 9 and 13 of Ref. 38) responsible for a transition from a single pulse localized state to a two-pulse state. The one qualitative difference between the Swift-Hohenberg equation and the present system lies in the ultimate fate of the two-pulse state. In the Swift-Hohenberg equation, this state reconnects with the trivial state in a subsequent primary bifurcation. In the present system, the two-pulse does not reconnect to the conduction state and instead exits the snaking region as shown in Fig. 4(b). This is likely a consequence of the choice of the aspect ratio of the domain, as explained in Ref. 39. Moreover, the continuous transition from a one-pulse solution to a two-pulse solution is a consequence of the no-slip boundary conditions at $x = \pm L/2$, i.e., of non-Neumann boundary conditions, just as in the Swift-Hohenberg equation.

B. Secondary snaking

The solutions described in Sec. III A are 3D analogues of the 2D localized states studied by Bergeon and Knobloch[17] in periodic domains with a large spatial period in the x direction. However, the presence of the third direction allows new types of behavior to take place, as well as changing the stability characteristics of the 2D solutions.

The most prominent and the most interesting consequence of the third dimension is the presence of secondary snaking. Secondary snaking arises from secondary bifurcations on the $L^\pm$ branches that break the D_2 symmetry of the localized states computed in the preceding section. These bifurcations always break the S_y symmetry and either S_c or $S_\triangle$ while respecting the remaining reflection symmetry. The presence of secondary symmetry-breaking bifurcations was noted already in earlier work on smaller enclosures[18] and their presence in the larger enclosure studied here is therefore not unexpected. Since such instabilities afflict each roll they are inherited by all localized states, regardless of their length. Consequently symmetry-breaking secondary bifurcations are expected to occur on every back and forth segment of the snaking branch. Figure 6 shows the eigenmodes responsible for these bifurcations.

Figure 7 shows the secondary branches we have computed. The branch L_1^+ in Fig. 7(a) is the result of a secondary instability with the eigenfunction shown in Fig. 6(a). This instability breaks the S_y and $S_\triangle$ symmetries of the L^+ branch and produces solutions with S_c symmetry. Likewise, instability with the eigenfunction in Fig. 6(b) breaks the symmetries S_y and S_c of the primary branch L^- and generates the secondary branch L_1^- of solutions with symmetry $S_\triangle$ (Fig. 7(b)). Subsequent secondary bifurcations (Figs. 6(c) and 6(d)) on the branch L^+ lead to the branches $L_{2\triangle}^+$ and L_{2c}^+ of $S_\triangle$-symmetric and S_c-symmetric solutions, respectively, and similarly for the L_1^- branch (Fig. 7(b)). We also see that all secondary snaking branches bifurcate supercritically from the $L^\pm$ branches and

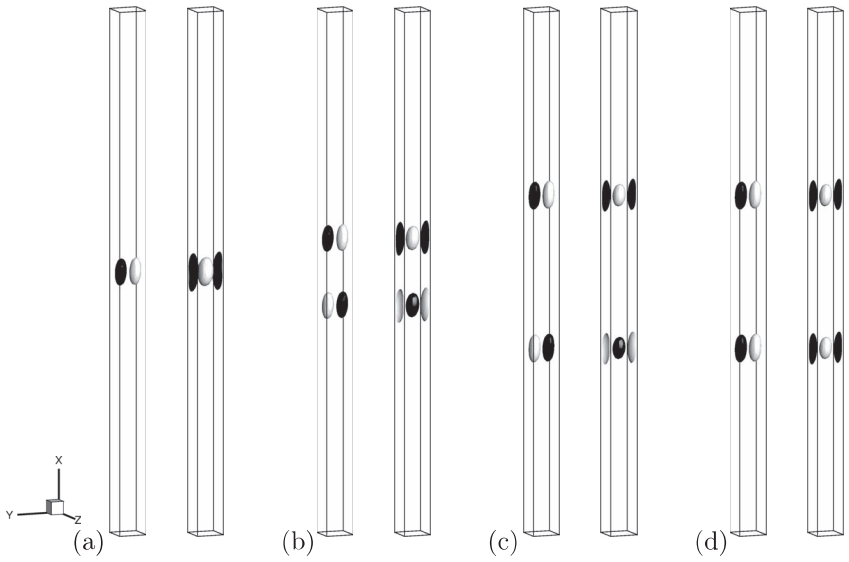

FIG. 6. Representation of the marginal eigenmode generating the branches (a) L_1^+ (S_c-symmetric), (b) L_1^- ($S_\triangle$-symmetric), (c) $L_{2\triangle}^+$ ($S_\triangle$-symmetric), and (d) L_{2c}^+ (S_c-symmetric) using a pair of equal and opposite isovalues of the vertical velocity (left panels) and of the z component of the vorticity (right panels). To reveal the twisting nature of the eigenmodes, the coordinate axes have been rotated with respect to earlier figures.

that a secondary snake is present on every back-and-forth segment of $L^\pm$. The snakes originate from the lower part of each such segment, as expected from the location of the corresponding bifurcation in small enclosures.[18] Figures 8 and 9 show snapshots of the resulting solutions at successive saddle-nodes along each of the six secondary branches shown in Fig. 7.

The first secondary bifurcation on L^+ is present at $Ra \approx 751.35$, before the branch passes the first saddle-node. This supercritical bifurcation generates the branch labeled L_1^+, which evolves into secondary snaking within the interval $745 < Ra < 819$. At the secondary bifurcation point, the solution consists of one small convection roll in the center of the domain (with a pair of weak rolls on either side) but since the branch bifurcates supercritically the resulting increase in Ra strengthens and enlarges this central roll. At the same time, the roll twists around the vertical axis breaking both S_y and S_c symmetries but preserving the $S_\triangle$ symmetry (Fig. 8(a)). After the first saddle-node at $Ra \approx 819$, the branch L_1^+ turns towards lower Rayleigh numbers and the solution nucleates two new rolls, one on either side of the existing roll. During the nucleation, the size and twist of the rolls decreases down to the left saddle-node but once the branch turns back towards higher Rayleigh

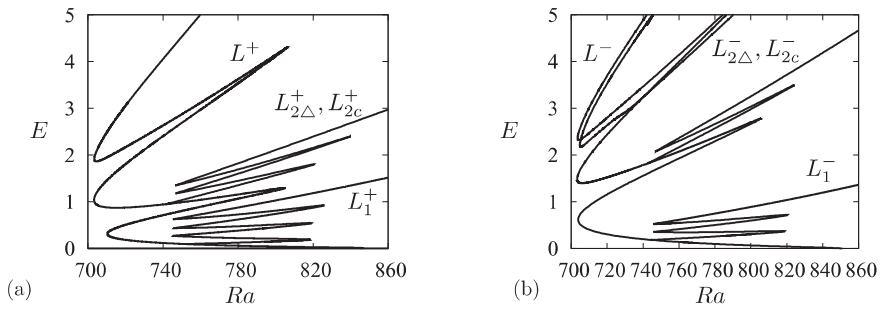

FIG. 7. Secondary snaking on the primary branches of localized states in terms of the kinetic energy E as a function of the Rayleigh number Ra. (a) L^+, (b) L^-. Secondary bifurcations occur on the subcritical parts of the primary branches and lead to the formation of localized twisted solutions represented by the secondary branches L_1^+, $L_{2\triangle}^+$, L_{2c}^+, L_1^-, $L_{2\triangle}^-$, and L_{2c}^-. Snapshots of these solutions are available in Figs. 8 and 9.

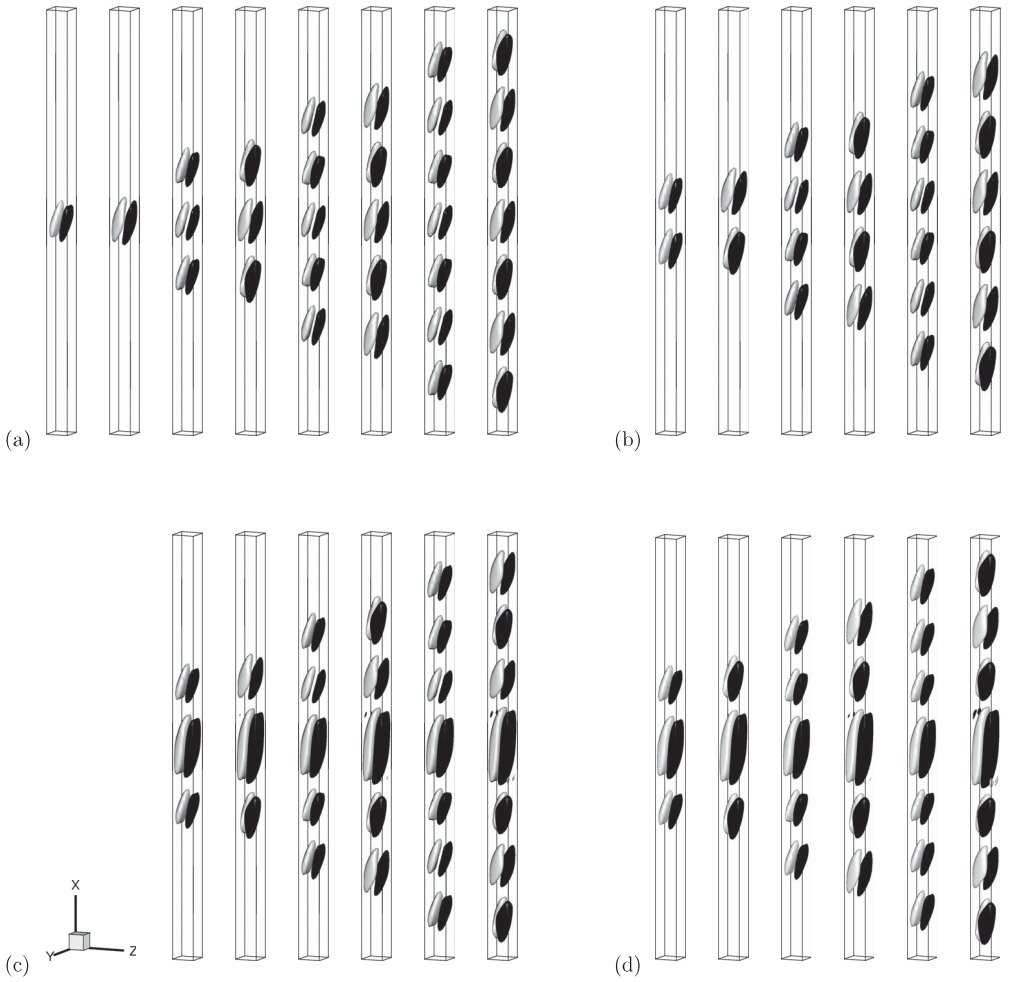

FIG. 8. Snapshots of the secondary branches of solutions shown in Fig. 7. The snapshots are taken at each saddle-node, beginning at the bifurcation point, and ending at a point on the right of the bifurcation diagram. The same representation as in Fig. 5 is employed. (a) Solutions on the L_1^+ branch (S_c symmetric, last snapshot at $Ra \approx 837$). (b) Solutions on the L_1^- branch ($S_\triangle$ symmetric, last snapshot at $Ra \approx 845$). (c) Solutions on the $L_{2\triangle}^+$ branch ($S_\triangle$ symmetric, last snapshot at $Ra \approx 862$). (d) Solutions on the L_{2c}^+ branch (S_c symmetric, last snapshot at $Ra \approx 864$).

numbers, the roll size increases again while the rolls twist alternately in opposite directions. This type of snaking continues until the solution consists of seven rolls (Fig. 8(a)), where the branch transitions towards large amplitude defect-like states, just like L^+. In fact, there are two such secondary snaking branches, with solutions of opposite twist. This sequence is repeated on the next subcritical segment, where two branches originate at $Ra \approx 742$ and are called $L_{2\triangle}^+$ and L_{2c}^+. This time, however, the central roll is larger than the rolls on either side (Figs. 8(c) and 8(d)). This is a consequence of the fact that the secondary branch bifurcates from a state consisting of a single roll that is in the process of nucleating side rolls. Consequently, all states on the $L_{2\triangle}^+$ and the L_{2c}^+ branches have a dominant central roll, followed by smaller rolls on either side as the structure nucleates additional rolls to fill the enclosure. During the snaking process, the large central roll remains untwisted but its size varies as expected: the roll is larger at the right saddle-nodes and smaller at the left saddle-nodes. However, the nucleated rolls at each back and forth oscillation twist and untwist in the same way as those on the L_1^+ branch. The $L_{2\triangle}^+$ and the L_{2c}^+ branches exit the snaking region once the solution consists of one large untwisted roll and six smaller twisted rolls. The difference in symmetry between $L_{2\triangle}^+$

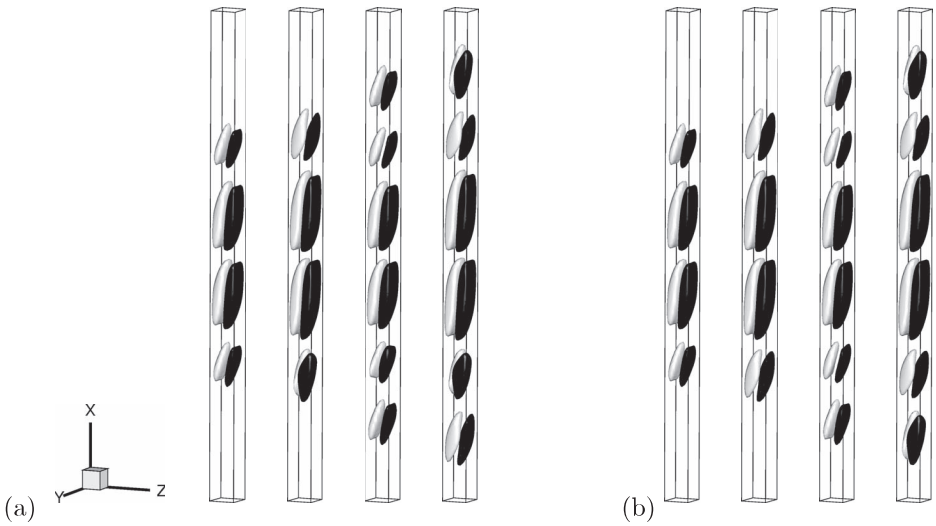

FIG. 9. As in Fig. 8 but for $L^-_{2\triangle}$ (a) and L^-_{2c} (b). Last snapshots are taken at $Ra \approx 836$ and $Ra \approx 832$, respectively.

and L^+_{2c} is highlighted in Figs. 10(a) and 10(b), where pairs of slices of the rightmost solutions in Figs. 8(c) and 8(d) are shown. The opposite twists associated with $L^+_{2\triangle}$ are easily discerned.

We also computed the first secondary bifurcation on the other primary branch of localized states, L^-. This bifurcation takes place at $Ra \approx 744$ and generates a secondary snaking branch referred to as L^-_1. This branch also bifurcates supercritically before undergoing a series of saddle-node bifurcations in the same Rayleigh number interval as L^+_1, $L^+_{2\triangle}$, and L^+_{2c}. This time, however, the localized structures contain an even number of rolls, starting with two rolls and exiting the snaking region when the structure consists of six rolls, but the same alternate twisting takes place along the structure (Fig. 8(b)) as takes place along the L^+_1 branch. Additional secondary branches bifurcating from L^- have also been computed: $L^-_{2\triangle}$ and L^-_{2c}. These solutions possess two large untwisted rolls in the center of the domain instead of one but otherwise behave like the $L^+_{2\triangle}$ and L^+_{2c} states described above (Fig. 9). The difference in symmetry between these states is illustrated in the slices shown in Figs. 10(c) and 10(d).

It is possible to understand the dominant features of both the bifurcation diagrams and of the associated solution snapshots. The key is provided by the eigenmodes shown in Fig. 6. Figure 6(a) shows that the instability to L^+_1 is associated with the loss of the symmetries S_y and $S_\triangle$. The remaining

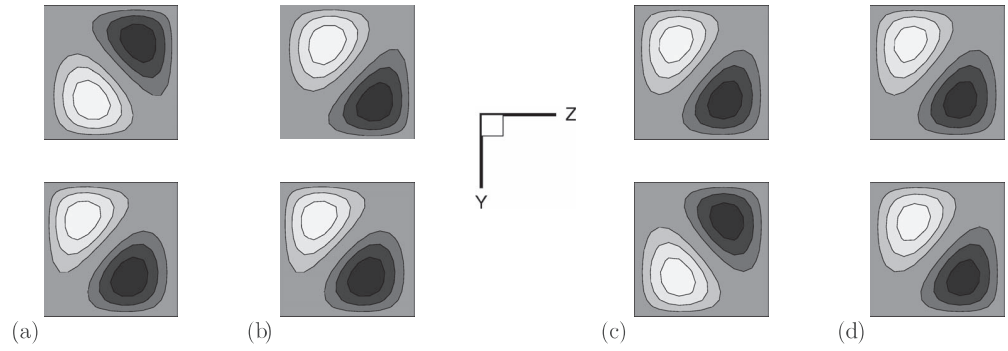

FIG. 10. Slices at $x = X$ (top) and $x = -X$ (bottom) of the rightmost states in Figs. 8(c) and 8(d) and 9(a) and 9(b), showing isovalues of the vertical velocity u, with dark/white indicating positive/negative values. (a) $L^+_{2\triangle}$. (b) L^+_{2c}. (c) $L^-_{2\triangle}$. (d) L^-_{2c}. In each case, X is chosen to capture the outermost rolls.

panels in the figure reveal that the secondary instabilities to L_1^-, $L_{2\triangle}^+$, and L_{2c}^+ take a similar form but that the instability is always confined to the two outermost rolls of the localized structure. The secondary instability therefore preserves the D_2-symmetric middle segment on the $L^\pm$ branches, and only twists the outermost rolls. As one proceeds up the $L^\pm$ branches, the instabilities associated with the outermost cells become more and more independent, and we can write the critical eigenmode in the form $\mathcal{U}(x+\ell/2) \pm \mathcal{U}(x-\ell/2)$, where $\mathcal{U}(x)$ is strongly peaked at $x=0$ and ℓ is the length of the D_2-symmetric convecton. The localization of the instability at $x = \pm\ell/2$ implies that the instabilities at opposite ends of the structure decouple to within exponentially small terms of order $\exp(-|\ell - 2x|/2\lambda)$, where λ is a constant of order the roll wavelength, cf. Ref. 41. It follows that the bifurcation to $L_{2\triangle}^+$ and L_{2c}^+ will occur at essentially the same Ra despite the different symmetries of these states. Indeed, our numerical simulations are unable to detect the exponentially small splitting of these bifurcations expected from the form of the associated eigenfunctions (Fig. 7). In addition, because the twisted state grows from the outermost rolls, the energies of the $L_{2\triangle}^+$ and L_{2c}^+ states are expected to be identical, again to within exponentially small terms, explaining why our computations do not detect a difference in energy between these two states (Fig. 7), despite the fact that they are not symmetry-related. In addition, we expect the secondary instabilities of $L^\pm$ to occur at essentially identical values of Ra, a consequence of the fact that the unstable mode is insensitive to the length of the structure. This fact is also borne out in Fig. 7. Moreover, only L_1^+ and L_1^- occur singly, a consequence of the fundamental difference in the eigenmodes in Figs. 6(a) and 6(b).

The snapshots in Fig. 8 allow us to make further predictions about the behavior of the associated solution branches. Figures 8(a) and 8(d) share the same symmetries but differ only in the presence of the central roll, which is substantially larger and stronger in the L_{2c}^+ solution than in the L_1^+ solution. The remaining rolls evolve in a very similar way along both branches (once the roll numbers are equal), while the central roll does not change. We expect therefore the two branches to look very similar in the bifurcation diagram, with the L_{2c}^+ displaced vertically by a fixed amount. This prediction works well at the left boundary of the snaking region, but less well at the right boundary. This is a consequence of the larger size of the central roll along L_{2c}^+ at this boundary; this increase in size implies that the outermost rolls are pushed closer to the no-slip endwalls at $x = \pm L/2$. Such rolls are therefore weaker and the Rayleigh number has therefore to be increased above and beyond that required to generate similar behavior in L_1^+, again in excellent qualitative agreement with Figs. 8(a) and 8(d). A similar discussion applies to the $S_\triangle$ states shown in Figs. 8(b) and 8(c) — these states only differ in the presence of the broad roll in the center of the localized structure in $L_{2\triangle}^+$ and its absence in L_1^-. Similar arguments apply to the solutions along the $L_{2\triangle}^-$ and L_{2c}^- branches (Figs. 9(a) and 9(b)).

IV. TIME-DEPENDENT DYNAMICS

In the classic snaking scenario, the solutions switch stability at successive saddle-nodes. However, the loss of stability of the primary quasi-two-dimensional structures with respect to fully three-dimensional disturbances creating the secondary snaking branches of twisted states implies that none of the primary states is likely to be stable. Moreover, the secondary branches bifurcate from unstable primary states and hence inherit their instability. As a result, no stable steady solutions have been found along either set of branches.

For this reason, we present here the results of typical time evolution computations for Rayleigh numbers beyond the primary transcritical bifurcation. We use a second order version of the time-stepping scheme used in our continuation code, with a timestep of 10^{-3} and confirm the results using a timestep of 10^{-4}.

The solution shown in Figs. 11(a) and 11(b), computed at $Ra = 900$, was initialized using a small perturbation of the conduction state in the form of the eigenvector associated with the transcritical bifurcation at $Ra_t \approx 850.86$. At this value of the Rayleigh number, the perturbation first creates a pair of rolls in the center of the container. As the amplitude of this roll pair grows, new rolls are added at either side, preserving the symmetries $S_\triangle$, S_y, and S_c of the solution. This nucleation and growth process continues until the solution fills the container with six rolls. However, the evolution

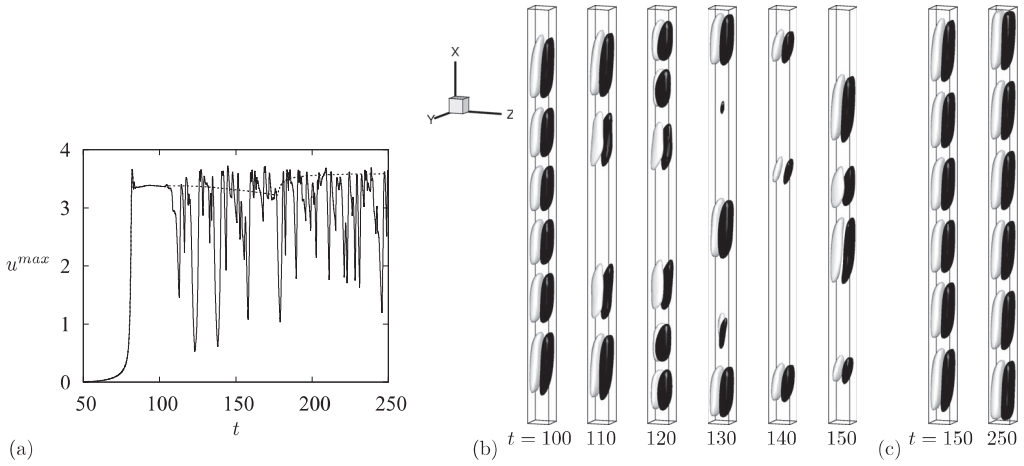

FIG. 11. (a) Time evolution at $Ra = 900$ of the maximum vertical velocity u^{max} from a small perturbation of the conduction state proportional to the eigenvector responsible from the transcritical bifurcation at $Ra = 850.86$. The dashed line shows the corresponding result with imposed S_y symmetry. (b) Solutions at several different times. (c) Solutions at $t = 150$ and $t = 250$ from the direct numerical simulation of Eqs. (2)–(5) with imposed S_y symmetry. All snapshots show isovalues of u as in Fig. 5.

does not stop. At $t = 110$, the 6-roll state is destabilized and the S_y and $S_\triangle$ symmetries are broken. The instability destroys the central rolls and the penultimate rolls on either side begin to twist. At $t = 130$, the solution no longer possesses any symmetry and evolves into an apparently chaotic state consisting of roll-like structures on various scales that repeatedly appear, spread and twist in an irregular manner before fading away again (Fig. 11(b)).

The loss of the S_y symmetry is crucial to the transition to the chaotic state. Figure 11(c) shows that when the S_y symmetry is imposed, the 6-roll state is stabilized and the final state (depicted at $t = 250$) persists to the end of the simulation (dashed line in Fig. 11(a)). This state forms when the nonuniform roll sizes depicted at $t = 150$ finally equalize. This readjustment is abrupt and takes place at $t \approx 175$. The resulting steady solution resembles the L^- state, and we conjecture that it lies on a disconnected part of the L^- branch as in Refs. 29 and 38. In contrast, if we instead impose one of the other reflection symmetries a chaotic final state remains. Simulations initiated by perturbing the conduction state with the eigenmode associated with the pitchfork bifurcation also result in a chaotic final state.

To examine the impact of the S_y symmetry, we also ran direct numerical simulations at $Ra = 810$ with and without imposing the S_y symmetry, in each case taking as initial condition a solution close to the second saddle-node along L^+ ($Ra \approx 804$). The results are reported in Fig. 12. With no symmetry imposed the initial roll starts to twist, breaking the S_y symmetry before decaying and spawning two untwisted rolls at $t \approx 40$. Figure 12(a) provides details of this evolution. These untwisted rolls subsequently decay and the twisted central roll is regenerated albeit smaller in size and weaker. After a further bounce, the solution decays to the conduction state, which is stable for $Ra \lesssim 850.78$. It is significant that the solution to the right of the pinning region decays to the conduction state instead of evolving to a spatially extended state as occurs in systems with gradient structure.

In contrast, when the symmetry S_y is imposed the dynamics is much slower (dashed lines in Fig. 12) with the nucleation of new rolls taking place at $t \approx 40$ and $t \approx 105$ (Fig. 12(a)). This time the final state that is reached is a steady solution with five rolls lying on the L^+ branch. The imposed symmetry stabilizes this state against the growth of perturbations breaking the S_y symmetry. In this case, the system behaves as expected of a gradient system to the right of the snaking region and the observed dynamics resemble those present in two dimensions.[17] Thus, the three-dimensionality of the structures studied here has a profound effect on the dynamics of doubly diffusive convection in a vertical cavity.

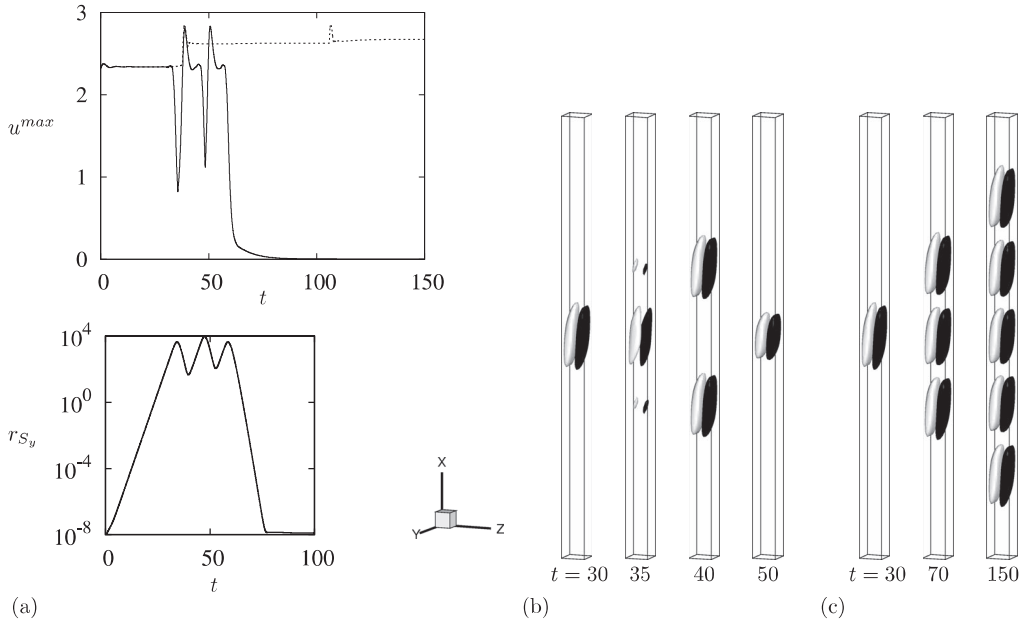

FIG. 12. (a) Time evolution at $Ra = 810$ of the maximum vertical velocity u^{max} starting from a solution at $Ra \approx 804$ close to the second saddle-node of L^+. The dashed line shows the corresponding result with imposed S_y symmetry. The lower panel shows the evolution of the asymmetry with respect to S_y using the L^2 norm $r_{S_y} \equiv \|\mathbf{f_y}\|_2$, where $\mathbf{f_y} \equiv (u, v, w, T, C) - S_y(u, v, w, T, C)$, measuring the difference between the solution and its image under S_y. When the symmetry S_y is not imposed, the solution decays to the conduction state. This is not the case when S_y imposed. Panels (b) and (c) show snapshots of the solution in these two cases. All snapshots show isovalues of u as in Fig. 5.

V. DISCUSSION

In this paper, we have computed for the first time fully three-dimensional localized states in natural doubly diffusive convection in a vertically extended enclosure with square cross-section. In the large aspect-ratio domains studied here, the quasi 2D states computed in Ref. 18 correspond to spatially localized states but continue to bifurcate directly from the conduction state. We have seen that these states are organized into a pair of snaking branches consisting of states with odd and even numbers of cells, and rather remarkably these behave very much like the corresponding states in the much simpler 1D Swift-Hohenberg equation on a finite interval with Robin boundary conditions.

We have also identified secondary instabilities on the snaking branches, analogous to those identified in Ref. 18, and showed that each of these leads to *secondary* snaking consisting of fully 3D spatially localized states. Similar secondary snaking has in fact been seen earlier in continuation studies of the 2D quadratic-cubic Swift-Hohenberg equation.[42] This system possesses a primary snaking branch of stripe-like states consisting of spots with hexagonal coordination (hereafter a *hexagonal pulse*). This snaking branch is present because of pinning of the front connecting the hexagonal pulse to the background homogeneous state to the hexagonal structure within. The secondary snaking is associated with the growth of a new row of spots along this front, i.e., it is associated with transverse growth as opposed to longitudinal growth, and therefore with pinning in the transverse direction. With Neumann boundary conditions in the transverse direction, the secondary snaking ceases once a complete row has been added, implying that the secondary snaking branch both originates and terminates in a transverse instability of a hexagonal pulse, i.e., the secondary branch initially breaks the symmetry of the hexagonal pulse, which is then restored when the secondary snake terminates. Thus, every back-and-forth oscillation of the primary snake is accompanied by a secondary snake connecting a lower part of the primary branch to the part right above.[42] Moreover, the secondary snakes originate in symmetry-breaking bifurcations close to the folds of the primary snake. Our results differ in two important aspects: in our problem the secondary snakes originate in secondary bifurcations far from the folds of the primary branch and

do not connect back to the primary snaking branch, i.e., symmetry is not restored as one follows the secondary snaking branch.

Like the 3D localized states computed recently for plane Couette flow,[27] our states are linearly unstable although we expect that they play a similar role in the transition to complex flow in this system. Indeed, the presence of the additional symmetry, introduced by the third dimension, is responsible for the presence of complex time-dependence at onset even in small domains.[18] In the present case, the system departs from gradient-type behavior as soon as this symmetry is not maintained. In addition, complex time behavior involving time-dependent localization and twisting is present beyond threshold, indicating that the time-independent solutions presented in Sec. III exert a considerable influence on the dynamics even when they are unstable.

In future work, we plan to examine the unbalanced case $N \neq -1$. Depending on the sign of $N+1$ this case is accompanied by a nontrivial base state with upflow along the hot boundary and downflow along the cold boundary or vice versa.[43,44] We anticipate therefore that the localized structures we have computed may be advected by the base flow resulting in new types of time-dependent behavior.

ACKNOWLEDGMENTS

This work was supported by the Action Thématique de l'Université Paul Sabatier (ATUPS) (C.B.), by CNES under GdR MFA 2799 "Micropesanteur Fondamentale et Appliquée" (C.B. and A.B.), and by the National Science Foundation (Grant Nos. DMS-0908102 and DMS-1211953) (E.K.). E.K. wishes to acknowledge support from the Chaire d'Excellence Pierre de Fermat de la région Midi-Pyrénées (France).

[1] E. Knobloch, D. R. Moore, J. Toomre, and N. O. Weiss, "Transitions to chaos in two-dimensional double-diffusive convection," J. Fluid Mech. **166**, 409–448 (1986).
[2] W. Barten, M. Lücke, M. Kamps, and R. Schmitz, "Convection in binary fluid mixtures. II. Localized traveling waves," Phys. Rev. E **51**, 5662–5680 (1995).
[3] A. Spina, J. Toomre, and E. Knobloch, "Confined states in large-aspect-ratio thermosolutal convection," Phys. Rev. E **57**, 524–545 (1998).
[4] O. Batiste and E. Knobloch, "Simulations of oscillatory convection in ^{3}He–^{4}He mixtures in moderate aspect ratio containers," Phys. Fluids **17**, 064102 (2005).
[5] C. Beaume, A. Bergeon, and E. Knobloch, "Homoclinic snaking of localized states in doubly diffusive convection," Phys. Fluids **23**, 094102 (2011).
[6] J. S. Turner, "The coupled turbulent transports of salt and heat across a sharp density interface," Int. J. Heat Mass Transfer **8**, 759–760 (1965).
[7] J. S. Turner, "Double diffusive phenomena," Annu. Rev. Fluid Mech. **6**, 37–54 (1974).
[8] J. S. Turner, "Multicomponent convection," Annu. Rev. Fluid Mech. **17**, 11–44 (1985).
[9] R. W. Schmitt, "Double diffusion in oceanography," Annu. Rev. Fluid Mech. **26**, 255–285 (1994).
[10] U. Hansen and D. A. Yuen, "Nonlinear physics of double-diffusive convection in geological systems," Earth-Sci. Rev. **29**, 385–399 (1990).
[11] E. Knobloch, "Nonlinear diffusive instabilities in differentially rotating stars," Geophys. Astrophys. Fluid Dyn. **22**, 133–158 (1982).
[12] N. Tsitverblit and E. Kit, "The multiplicity of steady flows in confined double-diffusive convection with lateral heating," Phys. Fluids A **5**, 1062–1064 (1993).
[13] N. Tsitverblit, "Bifurcation phenomena in confined thermosolutal convection with lateral heating: Commencement of the double-diffusive region," Phys. Fluids **7**, 718–736 (1995).
[14] S. Xin, P. Le Quéré, and L. S. Tuckerman, "Bifurcation analysis of double-diffusive convection with opposing horizontal thermal and solutal gradients," Phys. Fluids **10**, 850–858 (1998).
[15] W. R. Wilcox, "Transport phenomena in crystal growth from solution," Prog. Cryst. Growth Charact. Mater. **26**, 153–194 (1993).
[16] K. Ghorayeb and A. Mojtabi, "Double diffusive convection in a vertical rectangular cavity," Phys. Fluids **9**, 2339–2348 (1997).
[17] A. Bergeon and E. Knobloch, "Spatially localized states in natural doubly diffusive convection," Phys. Fluids **20**, 034102 (2008).
[18] A. Bergeon and E. Knobloch, "Natural doubly diffusive convection in three-dimensional enclosures," Phys. Fluids **14**, 3233–3250 (2002).
[19] J. Burke and E. Knobloch, "Localized states in the generalized Swift-Hohenberg equation," Phys. Rev. E **73**, 056211 (2006).
[20] J. Burke and E. Knobloch, "Snakes and ladders: Localized states in the Swift-Hohenberg equation," Phys. Lett. A **360**, 681–688 (2007).
[21] J. Burke and E. Knobloch, "Homoclinic snaking: Structure and stability," Chaos **17**, 037102 (2007).

[22] M. Beck, J. Knobloch, D. J. B. Lloyd, B. Sandstede, and T. Wagenknecht, "Snakes, ladders and isolas of localized patterns," SIAM J. Math. Anal. **41**, 936–972 (2009).
[23] G. W. Hunt, M. A. Peletier, A. R. Champneys, P. D. Woods, M. A. Wadee, C. J. Budd, and G. J. Lord, "Cellular buckling in long structures," Nonlinear Dyn. **21**, 3–29 (2000).
[24] D. V. Skryabin, "Instabilities of cavity solitons in optical parametric oscillators," Phys. Rev. E **60**, R3508–R3511 (1999).
[25] S. Blanchflower, "Magnetohydrodynamic convectons," Phys. Lett. A **261**, 74–81 (1999).
[26] D. Lo Jacono, A. Bergeon, and E. Knobloch, "Magnetohydrodynamic convectons," J. Fluid Mech. **687**, 595–605 (2011).
[27] T. M. Schneider, J. F. Gibson, and J. Burke, "Snakes and ladders: Localized solutions of plane Couette flow," Phys. Rev. Lett. **104**, 104501 (2010).
[28] D. Lo Jacono, A. Bergeon, and E. Knobloch, "Spatially localized binary fluid convection in a porous medium," Phys. Fluids **22**, 073601 (2010).
[29] I. Mercader, O. Batiste, A. Alonso, and E. Knobloch, "Convectons, anticonvectons and multiconvectons in binary fluid convection," J. Fluid Mech. **667**, 586–606 (2011).
[30] I. Mercader, O. Batiste, A. Alonso, and E. Knobloch, "Localized pinning states in closed containers: Homoclinic snaking without bistability," Phys. Rev. E **80**, 025201(R) (2009).
[31] L. S. Tuckerman, "Steady-state solving via Stokes preconditioning: Recursion relations for elliptic operators," in *Proceedings of the 11th International Conference on Numerical Methods in Fluid Dynamics*, edited by D. Dwoyer, M. Hussaini, and R. Voigt (Springer, Berlin, 1989), Lecture Notes in Physics 323, pp. 573–577.
[32] C. K. Mamun and L. S. Tuckerman, "Asymmetry and Hopf bifurcation in spherical Couette flow," Phys. Fluids **7**, 80–91 (1995).
[33] G. E. Karniadakis, M. Israeli, and S. A. Orszag, "High-order splitting methods for the incompressible Navier-Stokes equations," J. Comp. Phys. **97**, 414–443 (1991).
[34] D. Henry and H. Ben Hadid, "Multiple flow transitions in a box heated from the side in low-Prandtl-number fluids," Phys. Rev. E **76**, 016314 (2007).
[35] R. C. Paliwal and C. F. Chen, "Double-diffusive instability in an inclined fluid layer. Part 1. Experimental investigation," J. Fluid Mech. **98**, 755–768 (1980).
[36] R. C. Paliwal and C. F. Chen, "Double-diffusive instability in an inclined fluid layer. Part 2. Stability analysis," J. Fluid Mech. **98**, 769–785 (1980).
[37] S. Thangam, A. Zebib, and C. F. Chen, "Double-diffusive convection in an inclined fluid layer," J. Fluid Mech. **116**, 363–378 (1982).
[38] S. M. Houghton and E. Knobloch, "Homoclinic snaking in bounded domains," Phys. Rev. E **80**, 026210 (2009).
[39] A. Bergeon, J. Burke, E. Knobloch, and I. Mercader, "Eckhaus instability and homoclinic snaking," Phys. Rev. E **78**, 046201 (2008).
[40] I. Mercader, O. Batiste, A. Alonso, and E. Knobloch, "Convectons in periodic and bounded domains," Fluid Dyn. Res. **42**, 025505 (2010).
[41] J. Burke, S. M. Houghton, and E. Knobloch, "Swift-Hohenberg equation with broken reflection symmetry," Phys. Rev. E **80**, 036202 (2009).
[42] D. J. B. Lloyd, B. Sandstede, D. Avitabile, and A. R. Champneys, "Localized hexagons patterns of the planar Swift-Hohenberg equation," SIAM J. Appl. Dyn. Syst. **7**, 1049–1100 (2008).
[43] G. Bardan, A. Bergeon, E. Knobloch, and A. Mojtabi, "Nonlinear doubly diffusive convection in vertical enclosures," Physica D **138**, 91–113 (2000).
[44] S. A. Suslov and S. Paolucci, "Stability of non-Boussinesq convection via the complex Ginzburg-Landau model," Fluid Dyn. Res. **35**, 159–203 (2004).